Stephan C. Kaiser
Regine Eibl
Dieter Eibl

Zurich University of Applied Sciences, School of Life Sciences and Facility Management, Institute of Biotechnology, Campus Grüental, Wädenswil, Switzerland

Research Article

Engineering characteristics of a single-use stirred bioreactor at bench-scale: The Mobius CellReady 3L bioreactor as a case study

Stirred single-use bioreactors can be used as substitutes for their conventional counterparts made of glass or stainless steel in the development and production of biopharmaceuticals wherever possible. Various studies have confirmed their comparability in cell growth as well as in product quantity and quality. However, information about their engineering characteristics is still rare. This study focuses on the stirred Mobius® CellReady 3L bioreactor. The main engineering parameters for typical operation conditions used in animal cell cultivations are presented for the first time. Numerical simulations with a commercial CFD package (Fluent 6.3) were accomplished to obtain data on the single- and multi-phase fluid flow, power input, mixing time and oxygen mass transfer. The results, which were compared with data from experiments and from the literature, reveal the suitability of the Mobius® CellReady 3L bioreactor for cell expansion and protein production with animal cell cultures. Furthermore, the data enable comparisons with other single-use and reusable cell culture bioreactors at bench-scale.

Keywords: CFD / Engineering characteristics / Single-use bioreactor

Received: September 26, 2010; *revised:* January 20, 2011; *accepted:* March 16, 2011

DOI: 10.1002/elsc.201000171

1 Introduction

Stirred single-use (disposable) bioreactors, which have a flexible plastic cultivation vessel in contrast to their re-useable counterparts made of glass or stainless steel, have been commercially available since 2006. At that time, wave-mixed bag bioreactors (e.g. Wave Bioreactor from GE Healthcare or BioWave from Wavebiotech) dominated alongside well-known, stirred standard cell culture bioreactors. The broad acceptance of the wave systems can be explained by similar or even better results in cell cultivations, higher process flexibility, easy handling and reduced process costs [1]. Consequently, many producers of biopharmaceuticals have replaced roller and spinner flasks as well as stirred re-useable bioreactors for cell production at small and medium volume scale by wave-mixed systems, which were also established in process development and commercial vaccine productions [2]. However, with the exception of cell expansion and processes with shear sensitive cell cultures or foaming culture media, wave-mixed bag bioreactors are currently used less frequently than stirred single-use bioreactors. Hence, it is not surprising that the latter, which are available up to working volumes of 2 m^3, are the most commonly used single-use bioreactor systems today. Normally, their cultivation container is equipped with disposable or standard sensors to guarantee optimal process conditions for cell growth and product expression [3]. A comprehensive current overview describing the commercially available single-use bioreactors, their characteristics and recommended applications are given by Eibl et al. [1].

Nowadays, there are five stirred single-use bag systems for pilot and industrial scale (S.U.B.; BIOSTAT CultiBag STR; Nucleo Bioreactor; XDR-DSTB, animal; XDR-DSTB, microbial) and three laboratory-scale systems with rigid plastic vessels (Mobius CellReady 3L bioreactor, CelliGen® BLU SUB, SuperSpinner D1000) on the market. The introduction of the Mobius® CellReady 3L bioreactor in summer 2009 bridged the gap for stirred single-use bioreactors between laboratory and pilot scale. This unbaffled bioreactor has a rigid plastic cultivation vessel with a total volume of 3 L, in which mixing is guaranteed by a marine impeller. A micro-sparger is installed below the impeller for aeration.

For process development, comparability of single-use and conventional cell culture bioreactors is essential, especially when both systems have to be used side-by-side in hybrid solutions. A need for single-use bioreactors with design and set-up comparable to the reusable alternative is therefore

Correspondence: Stephan C. Kaiser (stephan.kaiser@zhaw.ch), Zurich University of Applied Sciences, School of Life Sciences and Facility Management, Institute of Biotechnology, Campus Grüental, P. O. Box, CH-8820 Wädenswil, Switzerland

Abbreviations: CFD, computational fluid dynamics; **MRF**, multiple reference frame

© 2011 WILEY-VCH Verlag GmbH & Co. KGaA, Weinheim

evident. However, literature data on engineering characteristics of single-use bioreactors are still rare and very few reports on hydrodynamic characteristics and oxygen mass transfer in stirred bag bioreactors (50 L, 200 L) can be found in the literature [4–6]. The advantageous usage of computational fluid dynamics (CFD) for the calculation of local and time-dependent flow velocities, concentration and temperature gradients as well as mixing intensities, shear stress and energy dissipation in single-use bioreactors have been highlighted [7].

First results of CFD investigations and cultivations with CHO suspension cells with the Mobius® CellReady 3L bioreactor were recently presented [1]. In this paper, the latest investigations of the Mobius CellReady's engineering characteristics are described and compared with other single-use and reusable cell culture bioreactors. The data presented can be used to realize scale-up strategies. In the experiments, process control was realized by ez-control (Applikon Biotechnology) with standard probes for pH, DO and temperature. To investigate the fluid flow pattern and its influence on mixing and oxygen mass transfer, simulations with a commercial CFD package (Fluent 6.3) were carried out. The multiple reference frame (MRF) method and a RANS approach were used to describe stirrer rotation and fluid flow.

2 Modeling approach and computational method

2.1 Single-phase modeling

For CFD modeling, the commercial CFD finite volume solver Fluent (version 6.3, ANSYS) was used. The numerical technique is based on the subdivision of the fluid domain into a finite number of control volumes and the discretization of the time-averaged mass and momentum equations. This provides algebraic equations that can be solved iteratively to render the solution field [8].

The Reynolds-averaged conservation equation for mass and momentum can be written as

$$\frac{\partial}{\partial t}+\nabla\cdot(\rho\cdot\vec{u})=0 \tag{1}$$

$$\frac{\partial(\rho\cdot\vec{u})}{\partial t}+\nabla\cdot(\rho\cdot\vec{u}\cdot\vec{u})=-\nabla p+\nabla\cdot(\bar{\bar{\tau}})+\vec{g}+\vec{F} \tag{2}$$

where ρ is the fluid viscosity, $\vec{u}$ is the velocity vector, p is the static pressure and the terms $\rho\cdot\vec{g}$ and $\vec{F}$ denote the gravitational and external body forces, respectively. The Reynolds stress tensor $\bar{\bar{\tau}}$ is described by the two-equation standard k–ε turbulence model, which is based on the Boussinesq hypothesis. This model assumes that turbulence responds fairly rapidly to changes in the mean flow, and thus relates the stress tensor $\bar{\bar{\tau}}$ to the mean velocity gradients as follows [9]:

$$\bar{\bar{\tau}}=\mu_t\cdot(\nabla\vec{u}+\nabla\vec{u}^{\mathrm{T}})-\frac{2}{3}\rho\cdot k\cdot\delta \tag{3}$$

The eddy viscosity μ_t is calculated with the turbulent kinetic energy k and the turbulent dissipation rate ε with the help of the turbulence parameter C_μ as follows [10]:

$$\mu_t=\rho\cdot C_\mu\cdot\frac{k^2}{\varepsilon} \tag{4}$$

The turbulence quantities are obtained by the following transport equations:

$$\frac{\partial(\rho\cdot k)}{\partial t}+\nabla\cdot(\rho\cdot k\cdot\vec{u})=\nabla\cdot\left[\left(\mu+\frac{\mu_t}{\sigma_k}\right)\cdot\nabla k\right]+G_k-\rho\cdot\varepsilon \tag{5}$$

$$\frac{\partial(\rho\cdot\varepsilon)}{\partial t}+\nabla\cdot(\rho\cdot\varepsilon\cdot\vec{u})=\nabla\cdot\left[\left(\mu+\frac{\mu_t}{\sigma_k}\right)\cdot\nabla\varepsilon\right]+C_{1\varepsilon}\cdot\frac{\varepsilon}{k}\cdot(G_k+C_{3\varepsilon}\cdot G_b)-C_{2\varepsilon}\cdot\rho\cdot\frac{\varepsilon^2}{k} \tag{6}$$

where the constants $C_{1\varepsilon}$, $C_{2\varepsilon}$, $C_{3\varepsilon}$, σ_k and σ_ε are equal to 1.42, 1.92, 0.45, 0.09, 1.0 and 1.3, respectively [11].

2.2 Multi-phase modeling

The multiphase simulations were carried out using the Euler–Euler approach, which considers water as continuous and air as the dispersed phase. The continuity equation for the kth phase can be written as

$$\frac{\partial(\alpha_k\cdot\rho_k)}{\partial \mathrm{t}}+\nabla\cdot(\alpha_k\cdot\rho_k\cdot\vec{\mathrm{u}}_k)=0 \tag{7}$$

where $\vec{u}_k$ is the phase velocity vector ($k=L$ the liquid phase and $k=G$ the gas phase), ρ_k is the phase density and α_k is the phase volume fraction. The phases are assumed to share space in proportion to their volume, so that their phase volume fractions sum to unity in the cell domain:

$$\sum_{i=1}^{n}\alpha_k=1 \tag{8}$$

The momentum conservation for multiphase flow is described by extended Navier–Stokes equations which can be written as

$$\frac{\partial(\alpha_k\cdot\rho_k\cdot\vec{u}_k)}{\partial t}+\nabla\cdot(\alpha_k\cdot\rho_k\cdot\vec{u}_k\cdot\vec{u}_k)=\nabla\cdot\tau_{\mathrm{eff},k}-\alpha_k\cdot\nabla p+\alpha_k\cdot\rho_k\cdot\vec{g}+\vec{F}_k+\vec{R}_k \tag{9}$$

The right-hand terms describe all the forces acting on the kth phase fluid element in the fluid domain. In addition to viscous stresses, the overall pressure gradient and gravitational force, interphase momentum forces $\vec{R}_k$ have to be taken into account. The most important interphase force is the drag force which acts on the bubbles resulting from the relative velocity between the two phases.

$$\vec{F}_{\mathrm{drag}}=\frac{3}{4}\rho_{\mathrm{L}}\cdot\alpha_{\mathrm{L}}\cdot\alpha_{\mathrm{G}}\cdot\frac{c_{\mathrm{D}}}{d_{\mathrm{B}}}\cdot|\vec{u}_{\mathrm{G}}-\vec{u}_{\mathrm{L}}|\cdot(\vec{u}_{\mathrm{G}}-\vec{u}_{\mathrm{L}}) \tag{10}$$

The drag coefficient c_{D} is calculated with the standard correlation given by Schiller and Naumann[12]:

$$c_{\mathrm{D}}=\begin{cases}\frac{24(1+0.15Re_{\mathrm{p}}^{0.687})}{Re_{\mathrm{p}}}, & Re_{\mathrm{p}}\le 1000\\ 0.44, & Re_{\mathrm{p}}\le 1000\end{cases} \tag{11}$$

© 2011 WILEY-VCH Verlag GmbH & Co. KGaA, Weinheim

The particle Reynolds number Re_p is defined as:

$$Re_p = \frac{\rho_L |\vec{u}_G - \vec{u}_L| \cdot d_B}{\eta_L} \quad (12)$$

Additionally, virtual mass $\vec{F}_{vm}$ was taken into account in this study using the default treatment included in Fluent, which can be written as [8]:

$$\vec{F}_{vm} = 0.5\ \rho_L \cdot \alpha_G \cdot \left(\frac{D\vec{u}_G}{Dt} - \frac{D\vec{u}_L}{Dt}\right) \quad (13)$$

The term $\vec{F}_k$ in Eq. (9) represents the Coriolis and centrifugal forces which are given for multi-phase flows by [13]:

$$\vec{F}_k = -2\alpha_k \cdot \rho_k \cdot \vec{N} \times \vec{u}_k - \alpha_k \cdot \rho_k \cdot \vec{N} \times (\vec{N} \times \vec{r}) \quad (14)$$

The Reynolds stress tensor for the gas–liquid system in Eq. (9) is calculated using the dispersed k–ε turbulence model, as the secondary phase is dilute and the primary phase is clearly continuous. The dispersed k–ε model predicts turbulence for the continuous phase using the standard k–ε turbulence model supplemented with extra terms that include interphase turbulent momentum transfer [8]. For the dispersed phase, turbulence quantities are obtained using the Tchen theory of dispersion of discrete particles by homogeneous turbulence [8]. The turbulent liquid viscosity is calculated analogous to the single-phase system using

$$\mu_{t,L} = \rho_L \cdot C_\mu \cdot \frac{k_L^2}{\varepsilon_L} \quad (15)$$

The transport equations for k_L and ε_L are given as

$$\frac{\partial}{\partial t}(\rho_L \cdot \alpha_L \cdot k_L) + \nabla \cdot (\rho_L \cdot \alpha_L \cdot \vec{u}_L \cdot k_L) = \nabla \cdot \left(\alpha_L \cdot \frac{\mu_{t,L}}{\sigma_k} \cdot \nabla k_L\right) + \alpha_L \cdot G_{kL} - \alpha_L \cdot \rho_L \cdot \varepsilon_L + \alpha_L \cdot \rho_L \cdot \Pi_{kL} \quad (16)$$

$$\frac{\partial}{\partial t}(\rho_L \cdot \alpha_L \cdot \varepsilon_L) + \nabla \cdot (\rho_L \cdot \alpha_L \cdot \vec{u}_L \cdot \varepsilon_L) = \nabla \cdot \left(\alpha_L \cdot \frac{\mu_{t,L}}{\sigma_k} \cdot \nabla \varepsilon_L\right) + \alpha_L \cdot \frac{\varepsilon_L}{k_L} \cdot (C_{1\varepsilon} \cdot G_{kL} - C_{2\varepsilon} \cdot \rho_L \cdot \varepsilon_L) + \alpha_L \cdot \rho_L \cdot \Pi_{\varepsilon L} \quad (17)$$

where G_{kL} represents the production rate of turbulent kinetic energy. The terms $\prod_{kL}$ and $\prod_{\varepsilon L}$ denote the influence of the interphase interaction, which are modeled following Rizk and Elgobashi [14]. All other parameters have the same meaning and values as in the single-phase k–ε turbulence model (see above).

2.3 Numerical details and boundary conditions

Simulations were realized for working volumes of 1.5, 2.0 and 2.5 liters. In each case, a hybrid mesh was generated using the preprocessor GAMBIT (version 2.4) as proposed by Naude et al. [15] and by Lu et al. [16]. Owing to the complex geometry and based on the accurate description of the impeller, the bottom and impeller zone were divided into unstructured tetrahedral cells. The bulk of the tank was meshed with structured hexahedral cells to decrease the cost of calculation. A previous grid sensitivity study had confirmed that the grids used with 306 000, 492 000 and 588 000 cells for the different fluid volumes show grid-independent results (data not shown).

The tank walls, the impeller and the probes were treated as non-slip boundaries with standard wall functions. The stirrer rotation was implemented using the MRF model, which is a good compromise between physical accuracy and reasonable computational effort. In steady simulations convergence was assumed when the residuals dropped below a value of 10^{-6}, and for transient cases a convergence criterion of 10^{-4} was chosen.

In multi-phase simulation, the higher order QUICK scheme was chosen for mass and momentum conservation equations. For pressure–velocity coupling the phase-coupled SIMPLE algorithm was used [8]. The gas flow rate at the sparger was defined via inlet-velocity boundary conditions with a gas volume fraction equal to unity. The inlet bubble diameter was assumed to be uniform and a value of 0.4 mm was defined, as observed in experiments. At the fluid surface, only gas was allowed to escape from the vessel. To reduce calculation time, single-phase flow field was used for initialization of multi-phase transient calculation [13].

3 Experimental investigations of mixing time and oxygen mass transfer

3.1 Bioreactor

The single-use Mobius® CellReady bioreactor has a rigid plastic tank with a dished bottom and a total volume of 3 L. The diameter of the unbaffled vessel is 0.137 with an *H/D* ratio of 1.82. Mixing is driven by a marine impeller with a diameter equal to 1/2 the tank diameter and an off-bottom clearance of 0.028 m. For aeration, a microsparger (sintered polyethylene, 15–30 μm pore size) is installed below the impeller.

3.2 Mixing time analysis

Mixing time was defined as the time required to achieve 95% homogeneity following addition of a tracer on the surface of the liquid [17]. The tracer was 1 M sodium thiosulfate, which was added instantaneously to a starchy iodine solution (10 g/L starch) by pipette. The measurement was performed for working volumes of 1.5, 2.0 and 2.5 L under non-aerated conditions. The agitation speed was varied at a range between 50 and 250 rpm, corresponding to tip speeds of 0.2 and 1 m/s, respectively. Each run was performed in triplicate. As the volume of each addition (200 μL) was less than 0.05% of the total volume, the effect on the volume change was negligible.

3.3 Oxygen mass transfer

The oxygen mass transfer coefficient k_La was determined using a dynamic method described by Kerdouss et al. [13]. The dissolved oxygen concentration was measured with a polarographic membrane oxygen probe (Mettler Toledo) and monitored with a computer interface. The measurement was taken in distilled water and in a 0.5 M Na_2SO_4 aqueous solu-

© 2011 WILEY-VCH Verlag GmbH & Co. KGaA, Weinheim

tion at 20°C, representing non-viscous coalescent and non-coalescent media, respectively. Aeration was varied in a range from 0.05 to 0.25 vvm, corresponding to superficial gas velocities of 1.13 and 5.65×10^{-4} m/s.

The k_La was determined from dissolved oxygen concentration measured as a function of time when aeration was turned on following complete oxygen removal by nitrogen. Assuming that the gas phase is well mixed and the dissolved oxygen concentration is uniform inside the liquid, the rate of oxygen transfer can be described by the following equation:

$$\mathrm{OTR} = \frac{\mathrm{d}c_{\mathrm{O_2}}}{\mathrm{d}t} = k_La \cdot (c^*_{\mathrm{O_2}} - c_{\mathrm{O_2}}) \tag{18}$$

where $c^*_{\mathrm{O_2}}$ is the saturation concentration given by Henry's law:

$$p_{\mathrm{O_2}} = H \cdot c^*_{\mathrm{O_2}} \tag{19}$$

By integration of Eq. 18 with $c_{\mathrm{O_2}}(t=0) = c_{\mathrm{O_2},0}$, the following equation is obtained:

$$\ln\left(\frac{c^*_{\mathrm{O_2}} - c_{\mathrm{O_2}}(t)}{c^*_{\mathrm{O_2}} - c_{\mathrm{O_2}},0}\right) = -k_La \cdot t \tag{20}$$

The k_La can be obtained as the slope when the left-hand side of Eq. (20) is plotted against time. The oxygen saturation concentration for the sodium sulfate solution was calculated in accordance with [18].

4 Results and discussion

4.1 Single-phase flow pattern

Figue 1 shows the flow pattern obtained at 2-L working volume. It is worth noting that the fluid velocity vectors are projected on the mid-tank plane for improved clearness, and therefore cannot represent a three-dimensional direction. Contrary to initial expectations, the single-phase simulations reveal no clear axial flow profile, but a dominance of the impeller's radial component for clockwise rotation. In this flow pattern the fluid is discharged toward the vessel wall, where the impeller discharge is divided and re-circulates in two flow loops per half of the vessel axially from the top and bottom to the stirrer (see Fig. 1). Owing to the pitch of the impeller blades, the impeller discharge is inclined toward the surface of the fluid at circa 25°. These results were qualitatively confirmed in experiments with the addition of small plastic particles to the fluid and visual observation of the particle trajectory (data not shown).

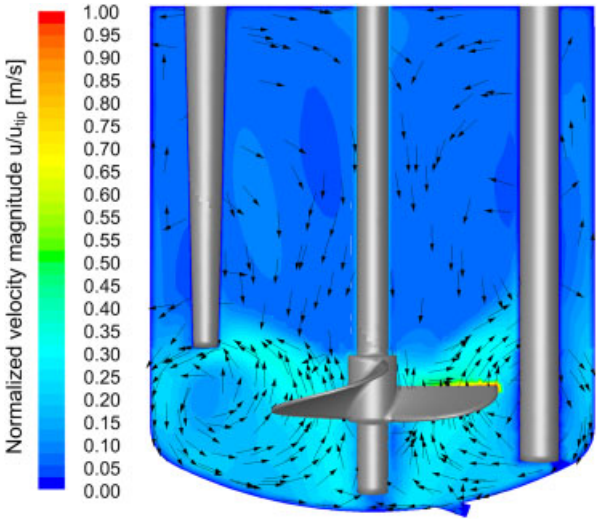

Figure 1. Fluid velocities in single-phase flow with 2.0 L working volume at 150 rpm. Velocity profiles are shown normalized by the tip speed as contour and vector plots for the *x*–*y*-plane.

As expected, the highest fluid velocities are found in close proximity to the impeller blades and correspond to the tip speed, which is defined as

$$u_{\mathrm{tip}} = \pi \cdot N_{\mathrm{R}} \cdot d_{\mathrm{R}} \tag{21}$$

The highest rotational speed of 250 rpm gives a tip speed of 0.997 m/s. In the simulation, the maximum fluid velocity was 0.989 m/s, which is very close to the theoretical value. The fluid velocities in the lower part of the vessel ($h < h_{\mathrm{F}}/2$) are primarily between 0.1 and 0.4 m/s. In the upper part of the vessel, considerably lower velocities with values below 10% of the tip speed are obtained. Thus, it can be argued that the impeller only has a small influence on this zone [19]. This effect is emphasized by an increasing filling level, which results in longer mixing times (see below). Xing et al. showed that inefficient mixing is accompanied by a decrease in oxygen mass transfer, which can induce oxygen concentration gradients in the case of bubble aeration [20]. Furthermore, a small dead zone is found in the inlet of the drain where the fluid velocities are nearly 0 m/s. In cultivation experiments with Chinese hamster ovary (CHO) suspension cells carried out in our laboratory, cell sedimentation and accumulation were observed in this region. The viability of these cells decreased significantly, which is probably the result of an insufficient nutrient and oxygen supply.

4.2 Power input

The power input was estimated by CFD as the momentum acting on the stirrer and the stirrer shaft, given by Eq. (22). In this study, no experimental determination of power input was carried out. Nevertheless, Lane and Koh and Patwardhan demonstrated that CFD-predicted and measured power inputs are in good agreement, the deviation being about 10% [21, 22]

$$P_{\mathrm{R}} = 2\pi \cdot M_{\mathrm{R}} \cdot N_{\mathrm{R}} \tag{22}$$

Depending on the working volume and stirrer speed, the volume-specific power input P/V varies in a range between 0.26 and 38.3 W/m^3 for 50 rpm (2.0 L) and 250 rpm (1.5 L) respectively. From the power input, the dimensionless power number (also known as the Newton number, Ne) is calculated as

$$Ne = \frac{P_{\mathrm{R}}}{\rho_{\mathrm{L}} \cdot N_{\mathrm{R}}^3 \cdot d_{\mathrm{R}}^5} \tag{23}$$

© 2011 WILEY-VCH Verlag GmbH & Co. KGaA, Weinheim

CFD simulations revealed that above a critical Reynolds number of $Re_{crit} \approx 10^4$ a full turbulent flow pattern is achieved in which the Newton number becomes constant with a value of 0.30. Although dominance of the impeller's radial component is indicated by the CFD simulation, the power number is comparable to typical axial pumping stirrers such as pitched-blade impellers or propeller stirrers as described by Liepe et al. [23]. Furthermore, although it is well known that the power number further decreases in unbaffled tanks as a result of a vortex formation, this phenomenon was not taken into account in the single-phase simulation. However, experimental determination of the stirrer torque realized by Millipore also reveals a power number of 0.31 for the investigated stirrer speeds (D. Kraus, Millipore Corporation, November 2009, personal communication), which matches the above-mentioned value very closely.

4.3 Mixing time

Mixing experiments show decreasing mixing times with increasing stirrer speeds. For 2.0 L working volume mixing times of 54.7 and 7.0 s are measured with tip speeds of 0.2 and 1.0 m/s, respectively. This is unsurprising because turbulence increases with higher rotational speed, which results in a higher mixing intensity [23, 24]. As already shown by the CFD simulations, the fluid velocity in the upper part of the vessel is rather low and the effect is more significant at higher filling levels. As a consequence, the mixing time increases significantly with higher working volumes due to the weakly mixed region near the liquid surface, where color remained the longest in the mixing experiments. Thus, with a tip speed of 0.2 m/s, the mixing time was 31.5 and 78.6 s for 1.5 and 2.5 L volume, respectively.

The mixing times measured can be correlated with the specific power input P/V predicted by the CFD simulations as suggested by Nienow [24]. Taking only cases with fully turbulent conditions and filling heights of $H_F/D \geq 1$ into account, the following correlation was found:

$$t_{95\%} = 26.54 \cdot (P/V)^{-0.36} \quad (24)$$

Based on turbulence theory, Nienow [24] suggests that the mixing time should be independent of impeller type and provides a correlation of the mixing time with the third radical of the specific power input (P/V), which is valid for vessels with H/D-ratios ≈ 1 and $Re > 10\,000$ [24]. The exponent of P/V found in this study is very close to the given value of $-1/3$ but, in order to achieve a defined mixing time, a higher specific power input is required in the bioreactor investigated than the correlation of Nienow [24], as shown in Fig. 2. Nevertheless, the dimensionless mixing number c_H (representing the number of stirrer rotations required to achieve the desired homogeneity) has a value of 34 ± 3.3 for fully turbulent conditions. Thus, the marine impeller is within the performance range of conventional stirrers such as the Rushton turbine or a $6 \times 45^\circ$ pitched-blade impeller, for which Liepe et al. reported c_H values of 24 and 30, respectively [23].

$$c_H = t_{95\%} \cdot N_R \quad (25)$$

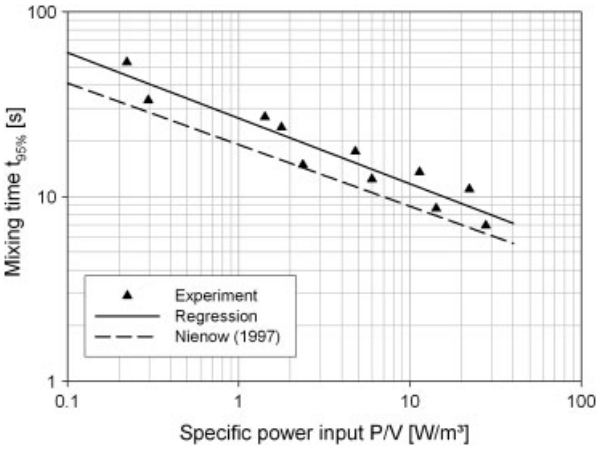

Figure 2. Measured mixing times as a function of specific power input predicted by CFD simulations. Experimental data are compared with a correlation provided by Nienow [24].

In CFD simulations, it is assumed that the tracer has identical fluid properties and does not influence the fluid flow pattern [25–28]. It is well known that the RANS approach underestimates the turbulent fluctuation of the flow field, which results in failure to predict reasonable tracer response curves [26, 28]. Nevertheless, good agreement between CFD-predicted and measured mixing times is usually achieved. In Table 1, the CFD-predicted mixing times are summarized and compared with the experimental data. In most cases, the mixing time calculated lies between or close to the measurement tolerance. Higher differences are only observed for a working volume of 1.5 L at 100 rpm and 2.5 L at 150 rpm.

4.4 Multiphase fluid flow pattern and gas distribution

The fluid flow pattern for a rotational speed of 150 rpm (equivalent to a tip speed of 0.6 m/s) and an aeration rate of 0.1 vvm is shown in Fig. 3. Owing to the low gassing rate, the shape of the flow pattern is not profoundly affected by the gas introduced. The dominance of the radial component is again obvious and the highest fluid velocities are found at the impeller tips. Small differences in fluid velocities between aerated and non-aerated cases are obtained below the impeller, because only low gas volume fractions (below 0.01%) are present in this region. As expected, significant effects of the gas introduced are detected near the gas inlet and in regions where the gas rises, which suggests that the flow is controlled not only by the impeller but also by the rising gas. In these regions, the fluid velocities were up to five times higher than those of the single-phase system and achieved values of $0.2\,u_{tip}$.

The spatial gas distribution is shown in Fig. 4. The greater part of the gas rises with low dispersion as the disruptive forces induced by the marine impeller rotation are insufficient to overcome buoyancy. This result has been qualitatively confirmed by visual observation, which revealed that the bubbles rise in a relatively undisturbed way through a confined

© 2011 WILEY-VCH Verlag GmbH & Co. KGaA, Weinheim

Table 1. Comparison of CFD-predicted mixing times with experimental data. Measured values are given as mean values of triplicates with the corresponding standard deviation

V (L)	N_R (rpm)	P/V (W/m^3)	$t_{95\%}$ (s)	
			CFD	Experiment
1.5	100	2.4	12.9	14.9 ± 0.9
1.5	150	8.0	7.0	7.3 ± 1.2
1.5	200	19.0	4.8	4.8 ± 0.2
1.5	250	37.0	3.9	3.4 ± 0.2
2.0	75	0.8	33.4	N.D.
2.0	100	1.8	22.3	23.7 ± 1.7
2.0	120	3.1	17.1	N.D.
2.0	150	6.0	11.8	12.4 ± 0.2
2.0	200	14.2	9.3	8.6 ± 0.7
2.0	250	27.8	8.8	7.0 ± 0.4
2.5	100	1.4	29.5	27.0 ± 1.8
2.5	150	11.4	21.7	17.5 ± 1.1
2.5	200	22.2	15.6	13.6 ± 1.6

N.D. – not determined.

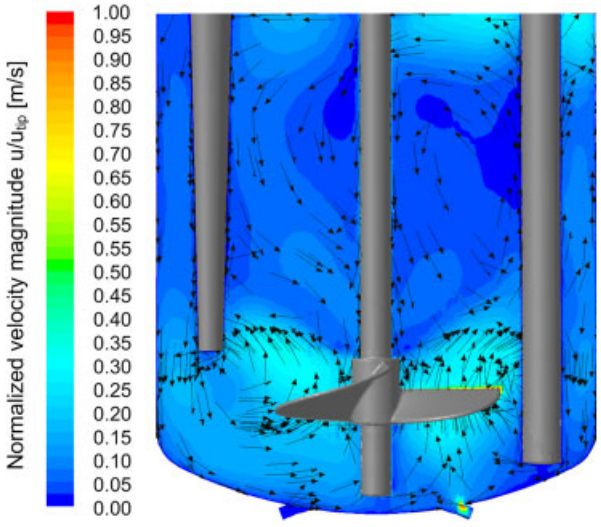

Figure 3. Fluid flow pattern under aeration condition with 0.1 vvm and a rotational speed of 150 rpm. The contour/vector plot is shown at the x–y-plane.

region above the impeller near the impeller shaft. The overall gas hold-up was highest at a stirrer speed of 200 rpm and an aeration rate of 0.1 vvm with a value of 0.155% (see Table 2). It is obvious that such small values cannot be observed experimentally from changes in the height of the liquid.

4.5 Oxygen mass transfer

4.5.1 Experimental results

It was observed in experiments that the bubble size in pure water was significantly larger than in the salt solution. The mean bubble size, which was obtained by photography, was about 2.1 ± 0.25 mm in pure water and 0.4 ± 0.05 mm in the salt solution. Owing to the larger bubbles, which have higher rising velocity due to their buoyancy force, the impeller was not able to distribute the bubbles in the reactor when pure water was used. Instead, the bubbles rose with little influence from the impeller. As a result, the oxygen mass transfer depends only on the aeration rate, but not on the stirrer speed (data not shown). Furthermore, the bubble size determined in Na_2SO_4 solution is more comparable with the bubble size observed in culture media during cultivation experiments.

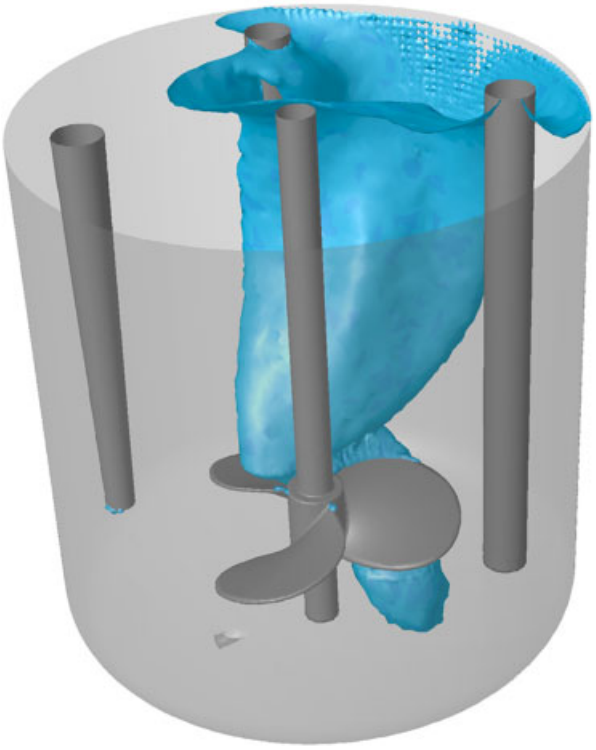

Figure 4. Spatial gas distribution under aeration condition with 0.1 vvm and a rotational speed of 150 rpm. The iso-surface represents a gas volume fraction of 0.05%.

Table 2. Results of the multi-phase simulations and comparison of CFD predicted mass transfer coefficients with experimental results for operation conditions investigated

N_R (rpm)	Q_G (vvm)	α_G (%)	a (m^{-1})	k_L (10^{-4} m/s)	k_La (h^{-1})	
					CFD	Experiment
100	0.05	0.092	13.8	1.88	5.32	6.8
100	0.10	0.142	21.3	2.05	8.47	8.3
150	0.05	0.144	14.4	2.19	5.56	6.5
150	0.10	0.145	21.7	2.32	9.11	13.0
200	0.05	0.144	21.4	2.46	7.16	7.6
200	0.10	0.155	23.3	2.59	9.85	11.8

The symbols N_R, Q_G, α_G, a, k_L and k_La represent the stirrer rotational speed, the aeration rate, the overall gas hold-up, the volume averaged gas–liquid surface area, the liquid mass transfer coefficient and the overall oxygen mass transfer coefficient, respectively.

© 2011 WILEY-VCH Verlag GmbH & Co. KGaA, Weinheim

Consequently, only results for oxygen mass transfer obtained with non-coalescent media are presented below.

In Fig. 5, mass transfer coefficients measured with different stirrer speeds are shown as a function of the aeration rate $\dot{Q}_G$ given as

$$\dot{Q}_G = \frac{F_G}{V_L} \tag{26}$$

where F_G is the gas volume flow rate. Clearly, the oxygen mass transfer depends on the aeration rate and the impeller speed, as expected [29, 30]. The highest k_La value is 35.9 h^{-1} for a rotational speed of 0.8 m/s and an aeration rate of 0.25 vvm. This value is slightly higher than results for the conventional stirred glass bioreactor Biostat BPlus 2L equipped with a ring sparger (Sartorius Stedim Biotech), for which k_La values up to 30 h^{-1} were obtained in our laboratory. Typical k_La values in animal cell cultures are in the range of 1 and 10 h^{-1} [30, 31]. The higher k_La value for the single-use bioreactor can be explained by the micro-sparger used producing smaller bubbles than a ring sparger. Corresponding to the reports of Zhang et al. and Nehring et al., micron-sized bubbles ensure oxygen transfer rates of up to 100 h^{-1} [32, 33]. However, different authors have reported that smaller bubbles cause greater cell damage than larger ones at the same volumetric air flow rate due to higher local energy dissipation at bubble rupture [34, 35]. Additionally, smaller bubbles lead to the generation of more stable foam layers on the surface of the liquid, and hence a higher demand for antifoam.

Based on the experimental results, an empirical model was set up which gives a correlation between the impeller tip speed u_{tip} (in m/s), aeration rate Q_G (in vvm) and the mass transfer coefficient k_La (in h^{-1}) in the range of operation investigated. The model approach is given by the following equation:

$$k_La = 4.249 - 10.61 \cdot u_{tip} + 60.0 \cdot Q_G + 4.606 \cdot u_{tip}^2 - 161.7 \cdot Q_G^2 + 160.4 \cdot u_{tip} \cdot Q_G \tag{27}$$

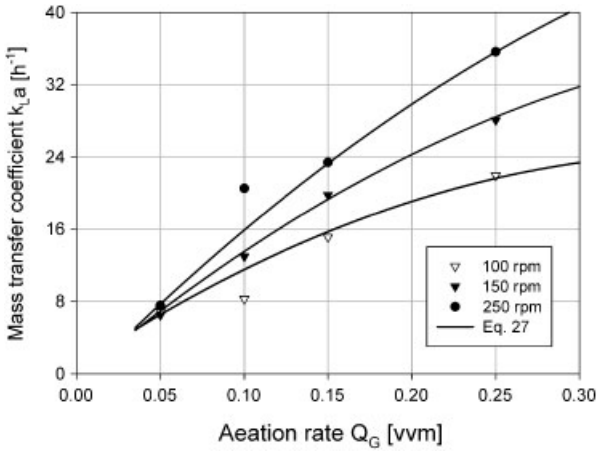

Figure 5. Experimental determined mass transfer coefficients in sodium sulfate solution for various operation conditions. The dots indicate measurements and the line plots represent the regression model (Eq. 27).

Good agreement is achieved between the statistical model and experimental data with a correlation coefficient of $R^2 = 0.97$. Mass transfer is enhanced by increasing impeller tip speed and aeration rate but, contrary to correlations given by Linek et al., the influence of the aeration rate is more significant [36]. This can be explained by higher gas hold-ups being achieved at higher aeration rates as the specific surface area increases (see Eq. 28). Although the overall gas volume fraction is also enhanced by higher impeller speed, the effect of the aeration is more significant in the range of operation investigated, as also indicated by CFD simulations (see Table 2).

4.5.2 Numerical results

Using the CFD simulation, the volumetric mass transfer coefficient k_La is calculated as the product of the liquid mass transfer coefficient k_L and the specific surface area a. Assuming spherical bubble shape, which is guaranteed up to a bubble diameter of 3 mm [37], the specific surface area a is calculated by:

$$a = \frac{6 \cdot \alpha_G}{d_B} \tag{28}$$

For the liquid mass transfer coefficient k_L the following correlation, which is based on Higbie's penetration theory, is given by Alves et al. [38]

$$k_L = C \cdot \sqrt{D_{O_2}} \cdot \left(\frac{\cdot}{L}\right)^{0.25} \tag{29}$$

where D_{O_2} is the diffusion coefficient (2.01×10^{-9} m^2/s at 20°C) and C is a constant with a value of 0.4. The volume-averaged values for the gas hold-up, the gas–liquid surface area, the liquid mass transfer coefficient and the overall oxygen mass transfer coefficient (see Table 2) were calculated according to [8]

$$\boldsymbol{\Phi} = \frac{1}{V} \cdot \int \boldsymbol{\Phi} dV = \frac{1}{V} \cdot \sum_{i=1}^{n} \boldsymbol{\Phi}_i \cdot |V_i| \tag{30}$$

where Φ, V_i and V represent the volume-averaged parameter, the cell volume and the total domain volume, respectively.

The highest local k_L values of up to 0.0023 m/s (for 150 rpm) were found near the impeller and the gas inlet, since the turbulence properties determining the surface renewal time for liquid film around the bubbles have the highest values in these regions. The overall k_L values were between 1.88×10^{-4} m/s and 2.59×10^{-4} m/s, depending on the stirrer speed and aeration rate (see Table 2). Thus, bearing in mind the heterogeneous spatial gas distribution, it can be argued that oxygen mass transfer also greatly depends on the location. Often this is only emphasized for large-scale bioreactors, but it also holds for bioreactors at laboratory scale.

Despite the assumption of a uniform bubble size, a comparison between CFD-predicted and the overall mass transfer coefficients measured shows good agreement (see Table 2). The mean variance was calculated as about 20%. Only in the case of 200 rpm and 0.1 vvm higher differences of about 40% were obtained. At higher stirrer speed, the turbulence inside the fluid is enhanced. Thus, a possible explanation for the deviation in the predicted k_La values could

© 2011 WILEY-VCH Verlag GmbH & Co. KGaA, Weinheim

be seen in the basic drag correlation by Schiller and Naumann [12], used in this work. This model only applies to bubbles moving in a quiescent liquid and does not apply to bubbles moving in turbulent liquid. Hence, modified drag laws that take into account the effect of turbulence are more favorable. A simple approach is the definition of a modified viscosity term in the relative Reynolds number as [13]

$$Re_p = \frac{\rho_L \cdot d_B \cdot |\vec{u}_L - \vec{u}_G|}{\mu_L + c_t \cdot \mu_{t,L}} \quad (31)$$

where μ_L is the laminar/molecular viscosity, $\mu_{t,L}$ is the turbulent viscosity, and c_t is a model parameter introduced to account for the effect of the turbulence in reducing slip velocity [39–41].

Furthermore, although bubble breakup phenomena are emphasized by increased turbulence, they are not considered in the CFD model presented. Various attempts to calculate bubble size distribution inside stirred vessels using population balance equations (PBE) are described in the literature [13, 39–43]. However, the computation using PBE becomes more complex and time consuming because additional transport equations for bubble size distribution are introduced into the simulation.

5 Concluding remarks

In this study, comprehensive experimental and numerical investigations for the determination of engineering parameters in the single-use Mobius® CellReady 3L bioreactor are presented. CFD simulations with a RANS approach and the MRF method revealed no clear axial fluid flow pattern but the dominance of the impeller's radial component in single and multi-phase flow. The CFD results show fully turbulent conditions above Reynolds numbers of circa 10^4, which correspond to a tip speed of about 0.4 m/s. Under such flow conditions, turbulent theory can be used to analyze the fluid mechanics in the bioreactor and constant values of 0.3 and 34 were obtained for the power number and dimensionless mixing time, respectively. These data indicate that the single-use marine impeller is in the performance range of conventional stirrers such as the Rushton turbine or pitched-blade impellers [23]. For the operation conditions investigated, the specific power input lies between 0.26 and 38.3 W/m^3, which is in the order of typical values given by Nienow[34] for cell culture bioreactors [34].

Multi-phase simulations with an Euler–Euler approach and a two-phase k–ε turbulence model revealed highly heterogeneous gas distribution and oxygen mass transfer. Although a uniform bubble size was assumed, good agreement between CFD-predicted and measured overall k_La were obtained. Depending on the stirrer speed and the aeration rate, the measured k_La were between 6.5 and 35 h^{-1} in Newtonian culture broths. Mobius® CellReady's determined k_La values were slightly higher than results for the stirred Biostat BPlus 2L (cell culture performance), the most frequently used re-usable system in our lab. It is assumed that the higher values found in the Mobius® CellReady arise from the microsparger installed in the single-use system, which produced smaller bubbles (of about 0.4 mm in diameter in sodium sulfate solution) compared with ring-sparger aeration systems.

In summary, it can be argued that the stirred single-use Mobius® CellReady 3L bioreactor shows comparable engineering characteristics to conventional cell culture bioreactors at bench-scale. Owing to the low mechanical stress, resulting from low specific power input and sufficient oxygen transfer capacity, the bioreactor is suitable for the cultivation of shear-sensitive cells with low to medium oxygen demands. Thus, it is not surprising that cell growth and protein production experiments with CHO and Hi-5™ suspension cells realized in our laboratory gained comparable results to those obtained from its reusable counterparts. Moreover, the data clearly indicate that the Mobius® CellReady 3L bioreactor represents a viable alternative to conventional cell culture bioreactors at bench-scale.

Nomenclature

a	[m^{-1}]	specific interphase area
c_D	[−]	drag coefficient
c_H	[−]	mixing number (dimensionless mixing time)
$c^*_{O_2}$	[kg/m^3]	liquid phase dissolved oxygen saturation concentration
c_{O_2}	[kg/m^3]	dissolved oxygen concentration in liquid phase
d_R	[m]	impeller diameter
d_B	[m]	bubble diameter
D	[m]	vessel diameter
D_{O_2}	[m^2/s]	oxygen diffusion coefficient
F	[N]	(external body) forces
F_G	[m^3/s]	gas flow rate
g	[9.81 m/s^2]	acceleration due to gravity
h	[m]	liquid height
H	[Pa kg^{-1} m^3]	Henry's constant
k	[m^2/s^2]	turbulent kinetic energy
k_L	[m/s]	liquid mass transfer coefficient
k_La	[s^{-1}]	specific oxygen mass transfer coefficient
M_R	[N m]	stirrer moment
N_R	[s^{-1}]	stirrer rotational speed
Ne	[−]	Power number (Newton number)
OTR	[kmol m^{-3} s^{-1}]	oxygen transfer rate
p	[Pa]	pressure
p_{O_2}	[Pa]	partial pressure of oxygen
P_R	[W]	impeller power input
Q_G	[vvm]	aeration rate
Re	[−]	Reynolds number
$t_{95\%}$	(s)	mixing time
u	[m/s]	velocity
u_{tip}	[m/s]	impeller tip speed
$\bar{v}_G$	[m/s]	superficial gas velocity
x, y, z	[m]	spatial coordinates
Greek letters		
α	[−]	phase volume fraction
δ_{ij}	[−]	Kronecker's symbol
ε	[m^2/s^3]	turbulent dissipation rate
μ	[Pa s]	viscosity
ρ	[m/s]	density
$\bar{\bar{\tau}}$	[kg m^{-1} s^{-2}]	stress tensor

The authors have declared no conflict of interest.

© 2011 WILEY-VCH Verlag GmbH & Co. KGaA, Weinheim

6 References

[1] Eibl, R., Kaiser, S., Lombriser, R., Eibl, D., Disposable bioreactors: the current state-of-the-art and recommended applications in biotechnology. *Appl. Microbiol. Biotechnol.* 2010, *86*, 41–49.

[2] Brecht, R., Disposable Bioreactors: Maturation into Pharmaceutical Glycoprotein Manufacturing. In Eibl, R., Eibl D. (Eds.), *Disposable Bioreactors*. Springer Series Advances in Biochemical Engineering/Biotechnology, *Vol. 115*, Springer, Berlin 2009, pp. 1–31.

[3] Rao, G., Moreira, A., Brorson, K., Disposable bioprocessing: the future has arrived. *Biotechnol. Bioeng.* 2009, *102*, 348–356.

[4] DeWilde, D., Noack, U., Kahlert, W., Barbaroux, M., Greller, G., Bridging the gap from reusable to single-use manufacturing with stirred, single-use bioreactors. *BioProcess Int.* 2009, *7*, 36–41.

[5] Eibl, R., Werner, S., Eibl, D., Disposable bioreactors for plant liquid cultures at L-scale: review. *Eng. Life Sci.* 2009, *9*, 156–164.

[6] Eibl, R., Eibl, D., Application of Disposable Bag Bioreactors in Tissue Engineering and for the Production of Therapeutic Agents, in: Kasper, G., van Griensven, M., Pörtner, R. (Eds.), *Bioreactor Systems for Tissue Engineering*. Springer Series Advances in Biochemical Engineering/Biotechnology, *Vol. 112*, Springer, Berlin 2009, pp. 183–207.

[7] Löffelholz, C., Kaiser, S. C., Werner, S., Eibl, D., CFD as a Tool to Characterize Single-use Bioreactors, in: Eibl, R., Eibl, D. (Eds.), *Single-use Technology in Biopharmaceutical Manufacture*, Wiley, NJ 2011.

[8] User's Manual to FLUENT 6.3, Centerra Resource Park, 10 Cavendish Court, Lebanon, USA, Fluent Inc., 2006.

[9] Paschedag A. R., *CFD in der Verfahrenstechnik allgemeine Grundlagen und mehrphasige Anwendungen*, Wiley, Weinheim 2004.

[10] Launder, B., Spalding, D., The numerical computation of turbulent flows. *Comp. Meth. Appl. Mech. Eng.* 1974, *3*, 269–289.

[11] Armenante, P., Chou, C.-C., Velocity profiles in a baffled vessel with single or double pitched-blade turbines. *AIChE J.* 1996, *42*, 42–54.

[12] Ishii, M., Zuber, N., Drag coefficient and relative velocity in bubbly, droplet or particulate flows. *AIChE J.* 1979, *25*, 843–855.

[13] Kerdouss, F., Bannari, A., Proulx, P., Bannari, R. et al., Two-phase mass transfer coefficient prediction in stirred vessel with a CFD model. *Comp. Chem. Eng.* 2008, *32*, 1943–1955.

[14] Rizk, M. A., Elgobashi, S. E., A two-equation turbulence model for dispersed dilute confined two-phase flows. *Int. J. Multiphase Flow* 1989, *15*, 119–133.

[15] Naude, I., Xuereb, C., Bewand, J., Direct prediction of the flows induced by a propeller in an agitated vessel using an unstructured mesh. *Can. J. Chem. Eng.* 1998, *76*, 631–640.

[16] Lu, Z. Y., Liao, Y., Qian, D. Y., Large eddy simulations of a stirred tank using the Lattice Boltzmann method on a nonuniform grid. *J. Comput. Phys.* 2002, *181*, 675–704.

[17] Hiraoka, S., Kato, Y., Tada, Y., Ozaki, N. et al., Power consumption and mixing time in an agitated vessel with double impeller. *Chem. Eng. Res. Des.* 2001, *79*, 805–810.

[18] Schumpe, A., Adler, I., Deckwer, W.-D., Solubility of oxygen in electrolyte solutions. *Biotechnol. Bioeng.* 1978, *20*, 145–150.

[19] Hockey, R. M., Nouri, J., Turbulent flow in a baffled vessel stirred by a 60° pitched blade impeller. *Chem. Eng. Sci.* 1996, *51*, 4405–4421.

[20] Xing, Z., Kenty, B. M., Li, Z. J., Lee, S. S., Scale-up analysis for a CHO cell culture process in large-scale bioreactors. *Biotechnol. Bioeng.* 2009, *103*, 733–746.

[21] Lane, G. L., Koh, P. T. L., CFD Simulation of a Rushton turbine in a baffled tank, *International Conference on CFD in Mineral and Metal Processing and Power Generation CSIRO* 1997, 377–385.

[22] Patwardhan, A., Prediction of flow characteristics and energy balance for a variety of downflow impellers. *Ind. Eng. Chem. Res.* 2001, *40*, 3806–3816.

[23] Liepe, F., Sperling, R., Jembere, S., *Rührwerke – Theoretische Grundlagen, Auslegung und Bewertung*. Eigenverlag FH Anhalt, Köthen 1998.

[24] Nienow, A. W., On impeller circulation and mixing effectiveness in the turbulent flow regime. *Chem. Eng. Sci.* 1997, *52*, 2557–2565.

[25] Jaworski, Z., Bujalski, W., Otomo, N., Nienow, A., CFD study of homogenization with dual rushton turbines – comparison with experimental results, Part I: initial studies. *Chem. Eng. Res. Des.* 2000, *78*, 327–333.

[26] Min, J., Gao, Z., Large eddy simulations of mixing time in a stirred tank. *Chin. J. Chem. Eng.* 2006, *14*, 1–7.

[27] Zadghaffari, R., Moghaddas, J., Revstedt, J., A mixing study in a double-Rushton stirred tank. *Comp. Chem. Eng.* 2009, *33*, 1240–1246.

[28] Jahoda, M., Mostek, M., Kukuková, A., Machon, V., CFD modelling of liquid homogenization in stirred tanks with one and two impellers using large eddy simulation. *Chem. Eng. Res. Des.* 2007, *85*, 616–625.

[29] Van't Riet, K., Review of measuring methods and results in nonviscous gas–liquid mass transfer in stirred vessels. *Ind. Eng. Chem. Process Des. Dev.* 1979, *18*, 357–364.

[30] Henzler, H.-J., Kauling, D. J., Oxygenation of cell cultures. *Bioprocess Biosys. Eng.* 1993, *9*, 61–75.

[31] Langheinrich, C., Nienow, A. W., Eddleston, T., Stevenson, N. C. et al., Oxygen transfer in stirred bioreactors under animal cell culture conditions. *Food Bioprod. Process.* 2002, *80*, 39–44.

[32] Zhang, S., Handa-Corrigan, A., Spier, R. E., Oxygen transfer properties of bubbles in animal cell culture media. *Biotechnol. Bioeng.* 1992, *40*, 252–259.

[33] Nehring, D., Czermak, P., Vorlop, J., Lübben, H., Experimental study of a ceramic microsparging aeration system in a pilot-scale animal cell culture. *Biotechnol. Prog.* 2004, *20*, 1710–1717.

[34] Nienow, A. W., Reactor engineering in large scale animal cell culture. *Cytotechnology* 2006, *50*, 9–33.

[35] Chisti, Y., Animal-cell damage in sparged bioreactors. *Trends Biotechnol.* 2000, *18*, 420–432.

© 2011 WILEY-VCH Verlag GmbH & Co. KGaA, Weinheim

[36] Linek, V., Vacek, V., Benes, P., A critical review and experimental verification of the correct use of the dynamic method for the determination of oxygen transfer in aerated agitated vessels to water, electrolyte solutions and viscous liquids. *Chem. Eng. J.* 1987, *34*, 11–34.

[37] Gimbun, J., Rielly, C., Nagy, Z., Modelling of mass transfer in gas–liquid stirred tanks agitated by Rushton turbine and CD-6 impeller: a scale-up study. *Chem. Eng. Res. Des.* 2009, *87*, 437–451.

[38] Alves, S., Vasconcelos, J., Orvalho, S., Mass transfer to clean bubbles at low turbulent energy dissipation. *Chem. Eng. Sci.* 2006, *61*, 1334–1337.

[39] Kerdouss, F., Bannari, A., Proulx, P., CFD modeling of gas dispersion and bubble size in a double turbine stirred tank. *Chem. Eng. Sci.* 2006, *61*, 3313–3322.

[40] Laakkonen, M., Alopaeus, V., Aittamassa, J., Validation of bubble breakage, coalescence and mass transfer models for gas–liquid dispersion in agitated vessel. *Chem. Eng. Sci.* 2006, *61*, 218–228.

[41] Lane, G. L., Schwarz, M. P., Evans, G. M., Numerical modeling of gas–liquid flow in stirred tank. *Chem. Eng. Sci.* 2005, *60*, 2203–2214.

[42] Dhanasekharan, K., Sanyal, J., Jain, A., Haidari, A., A generalized approach to model oxygen transfer in bioreactors using population balances and computational fluid dynamics. *Chem. Eng. Sci.* 2005, *60*, 213–218.

[43] Zhang, H., Zhang, K., Fan, S., CFD simulation coupled with population balance equations for aerated stirred bioreactors. *Eng. Life Sci.* 2009, *9*, 421–430.

© 2011 WILEY-VCH Verlag GmbH & Co. KGaA, Weinheim